Chemical Science

EDGE ARTICLE

View Article Online
View Journal | View Issue

Check for updates

Cite this: *Chem. Sci.*, 2018, **9**, 2952

Positional effects of second-sphere amide pendants on electrochemical CO_2 reduction catalyzed by iron porphyrins†

Eva M. Nichols,‡[ab] Jeffrey S. Derrick,‡[ab] Sepand K. Nistanaki,[a] Peter T. Smith[ab] and Christopher J. Chang *[abcd]

The development of catalysts for electrochemical reduction of carbon dioxide offers an attractive approach to transforming this greenhouse gas into value-added carbon products with sustainable energy input. Inspired by natural bioinorganic systems that feature precisely positioned hydrogen-bond donors in the secondary coordination sphere to direct chemical transformations occurring at redox-active metal centers, we now report the design, synthesis, and characterization of a series of iron tetraphenylporphyrin (**Fe-TPP**) derivatives bearing amide pendants at various positions at the periphery of the metal core. Proper positioning of the amide pendants greatly affects the electrocatalytic activity for carbon dioxide reduction to carbon monoxide. In particular, derivatives bearing proximal and distal amide pendants on the *ortho* position of the phenyl ring exhibit significantly larger turnover frequencies (TOF) compared to the analogous *para*-functionalized amide isomers or unfunctionalized **Fe-TPP**. Analysis of TOF as a function of catalyst standard reduction potential enables first-sphere electronic effects to be disentangled from second-sphere through-space interactions, suggesting that the *ortho*-functionalized porphyrins can utilize the latter second-sphere property to promote CO_2 reduction. Indeed, the distally-functionalized *ortho*-amide isomer shows a significantly larger through-space interaction than its proximal *ortho*-amide analogue. These data establish that proper positioning of secondary coordination sphere groups is an effective design element for breaking electronic scaling relationships that are often observed in electrochemical CO_2 reduction.

Received 30th October 2017
Accepted 14th February 2018

DOI: 10.1039/c7sc04682k

rsc.li/chemical-science

Open Access Article. Published on 21 2018. Downloaded on 16.10.2025 18:37:00.
This article is licensed under a Creative Commons Attribution-NonCommercial 3.0 Unported Licence.

Introduction

Environmental challenges associated with rising atmospheric CO_2 concentrations and the promise of CO_2 as a cheap and abundant C1 feedstock motivate the research into technologies to convert CO_2 into value-added chemical products.[1–3] Electrochemical reduction of CO_2 offers an attractive approach to meet this goal using sustainable energy input, but the kinetic and thermodynamic barriers to CO_2 activation provide significant chemical challenges, necessitating the development of catalysts that can promote CO_2 reduction selectively over the competing background reduction of protons to hydrogen that can occur at comparable potentials. Indeed, despite broad interest in electrochemical CO_2 reduction, molecular catalysis efforts have focused largely on a limited number of primary coordination sphere motifs, including metal complexes with porphyrins[4–8] and aza-macrocycles,[9–15] bipyridine,[16–23] phosphine,[24–26] and carbene[27–29] ligands. In contrast, biological systems for CO_2 redox catalysis, such as the carbon monoxide dehydrogenase (CODH) enzymes that catalyze the reversible interconversion of CO_2 and CO, modulate activity using precisely positioned hydrogen-bond and proton-relay groups in the second coordination sphere.[30] For example, second-sphere histidine and lysine residues in Ni–Fe CODH are positioned to stabilize a CO_2-metal adduct and assist in C–O bond cleavage (Scheme 1).[31–33]

The aforementioned bioinorganic systems provide inspiration for the design of metal complexes bearing second-sphere groups to aid with activation or transformation of small molecule substrates. Notable advances in utilizing intramolecular hydrogen-bond donors to promote oxygen binding/activation include picket fence-, picnic basket-, and hangman porphyrins by Collman, Reed, C. K. Chang, and Nocera,[34–39] dicopper complexes by Masuda,[40,41] and tripodal systems by Borovik.[42–45] Second-sphere donors have also been shown to play important

[a]*Department of Chemistry, University of California, Berkeley, CA 94720, USA. E-mail: chrischang@berkeley.edu*

[b]*Chemical Sciences Division, Lawrence Berkeley National Laboratory, Berkeley, CA 94720, USA*

[c]*Department of Molecular and Cell Biology, University of California, Berkeley, CA 94720, USA*

[d]*Howard Hughes Medical Institute, University of California, Berkeley, CA 94720, USA*

† Electronic supplementary information (ESI) available: Procedures for synthetic, spectroscopic, and electrochemical experiments. CCDC 1582750. For ESI and crystallographic data in CIF or other electronic format see DOI: 10.1039/c7sc04682k

‡ These authors contributed equally to this work.

This journal is © The Royal Society of Chemistry 2018

Open Access Article. Published on 21 2018. Downloaded on 16.10.2025 18:37:00.
This article is licensed under a Creative Commons Attribution-NonCommercial 3.0 Unported Licence.

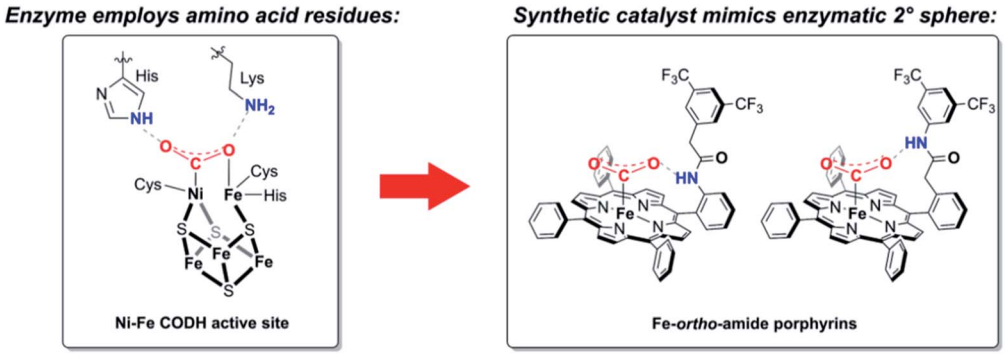

Scheme 1 The active site of Ni–Fe CO dehydrogenase, showing activated CO_2 in red and the nearby network of hydrogen bond donor amino acid residues in blue (left), inspires the design of *ortho*-amide-functionalized Fe porphyrins examined in this work (right).

roles in structural mimics of alcohol dehydrogenase,[46,47] as well as in complexes for stoichiometric reduction of nitrite,[48,49] nitrate,[50] and nitrogen.[51] Furthermore, second-sphere pendants have been incorporated into electrocatalyst scaffolds to facilitate protonation steps relevant to H_2 evolution[52–54] and O_2 reduction,[55,56] and to stabilize adducts or promote C–O bond cleavage in CO_2 reduction.[11,12,57–59] With specific regard to CO_2 reduction, elegant work on iron tetraphenylporphyrins by Savéant, Costentin, and Robert has explored the use of phenol-based pendants for enhancing electrochemical CO_2 reduction.[57,60]

Against this backdrop, we targeted the study of functionalized porphyrin complexes that could yield insight into questions of optimal placement of second-sphere pendants on a conserved first-sphere metal core. In this report, we describe the synthesis and electrochemical study of positional isomers of iron porphyrin CO_2 reduction catalysts bearing pendant amides in the secondary coordination sphere. Intermolecular addition of a parent iron tetraphenylporphyrin catalyst, **Fe-TPP**, with an aryl amide additive results in a dose-dependent increase in CO_2 reduction activity. Building upon this result, we designed and evaluated a series of positional isomers bearing intramolecular amide pendants in the *ortho* or *para* positions of the *meso* aryl ring, both proximal and distal to the porphyrin plane. Comparison of the catalytic activities of these isomers establishes that *ortho* orientation of the second-sphere groups is critical for an enhancement in catalysis. Correlation between the turnover frequency (TOF) and standard potential of the formal $Fe^{I/0}$ couple indicates that through-space interactions play a role in enhancing the rate of CO_2 reduction for both *ortho* amide-functionalized catalysts, with the distal donor exhibiting a more significant through-space component. In contrast, such effects are largely absent in the *para*-functionalized congeners. These data provide a starting point for more sophisticated design of second-sphere functionalities as bioinspired design elements for redox catalysis of CO_2 and other small-molecule substrates.

Results and discussion

Bis(aryl)amide additive promotes CO_2 reduction with Fe porphyrin

As a starting point to explore the use of amides as functional secondary coordination sphere pendants, we examined the effects of an electron-deficient aryl amide additive on CO_2 reduction catalyzed by **Fe-TPP**. Titration of 3,5-[bis(trifluoromethyl)phenyl]amide to **Fe-TPP** in dimethylformamide (DMF) reveals a dose-dependent increase in catalytic activity (Fig. 1), with the additive acting as a proton source as well as a potential hydrogen bond donor/acceptor. Foot-of-the-wave analysis (FOWA), as described by Savéant, Costentin, Robert and co-workers,[61] can be used to extract kinetic information from cyclic voltammetric data, especially in cases where a plateau current is not observed due to substrate consumption or catalyst inhibition. Using this approach, the rate of CO_2 reduction was examined as a function of amide concentration under pseudo-first order conditions of excess CO_2, and the rate was found to exhibit a first-order dependence on the amide additive (Fig. S1†). Cyclic voltammograms under a nitrogen atmosphere show a negligible change between 50 equivalents of amide additive and **Fe-TPP** alone, indicating that background processes such as proton reduction are likely to be minimal with this additive (Fig. S2†). With this pilot result in hand, we sought to explore the effects of introducing intramolecular amide substituents onto the porphyrin scaffold in a spatially well-defined fashion.

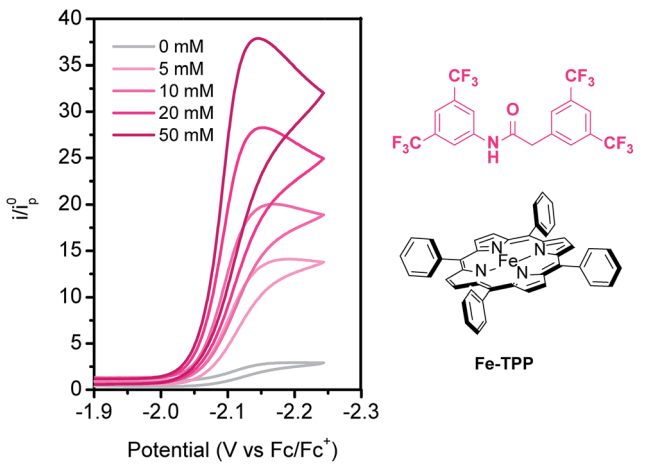

Fig. 1 Titration of 3,5-[bis(trifluoromethyl)phenyl]amide to **Fe-TPP** under CO_2 showing current increases with increasing concentrations of amide. Conditions: 0.1 M $TBAPF_6$ in DMF, 1 mM **Fe-TPP**.

Open Access Article. Published on 21 2018. Downloaded on 16.10.2025 18:37:00.
This article is licensed under a Creative Commons Attribution-NonCommercial 3.0 Unported Licence.

Synthesis of covalently-modified porphyrins bearing intramolecular amide groups

As only amide groups located at the *ortho* position of the porphyrin *meso* aryl rings are expected to engage in intramolecular proton donor- or hydrogen bonding interactions with CO_2-derived intermediates bound at the iron center, we envisioned two positional isomers: ***ortho*-1-amide**, bearing the NH proximal to the porphyrin ring, and ***ortho*-2-amide**, bearing the NH distal to the porphyrin ring. Most porphyrin-based catalysts bearing second-sphere groups, especially those evaluated for CO_2 reduction, feature these functionalities in the proximal location for reasons of synthetic practicality. We were interested in interrogating the effect of distal group positioning given a previous report showing that proximal second-sphere groups are located too far away from the metal center and are less effective at promoting oxygen binding at iron.[36] The corresponding ***para*-1-amide** and ***para*-2-amide** porphyrins were targeted to serve as control compounds, where the amide NH group at the *para* position of the *meso* aryl rings is not expected to interact productively with CO_2 or CO_2-derived intermediates. The synthesis of all four functionalized porphyrin ligands is shown in Scheme 2.

Condensation of 2-nitrobenzaldehyde and benzaldehyde with pyrrole results in the mono-(2-nitrophenyl)porphyrin starting material **1**, which can be subsequently reduced to the

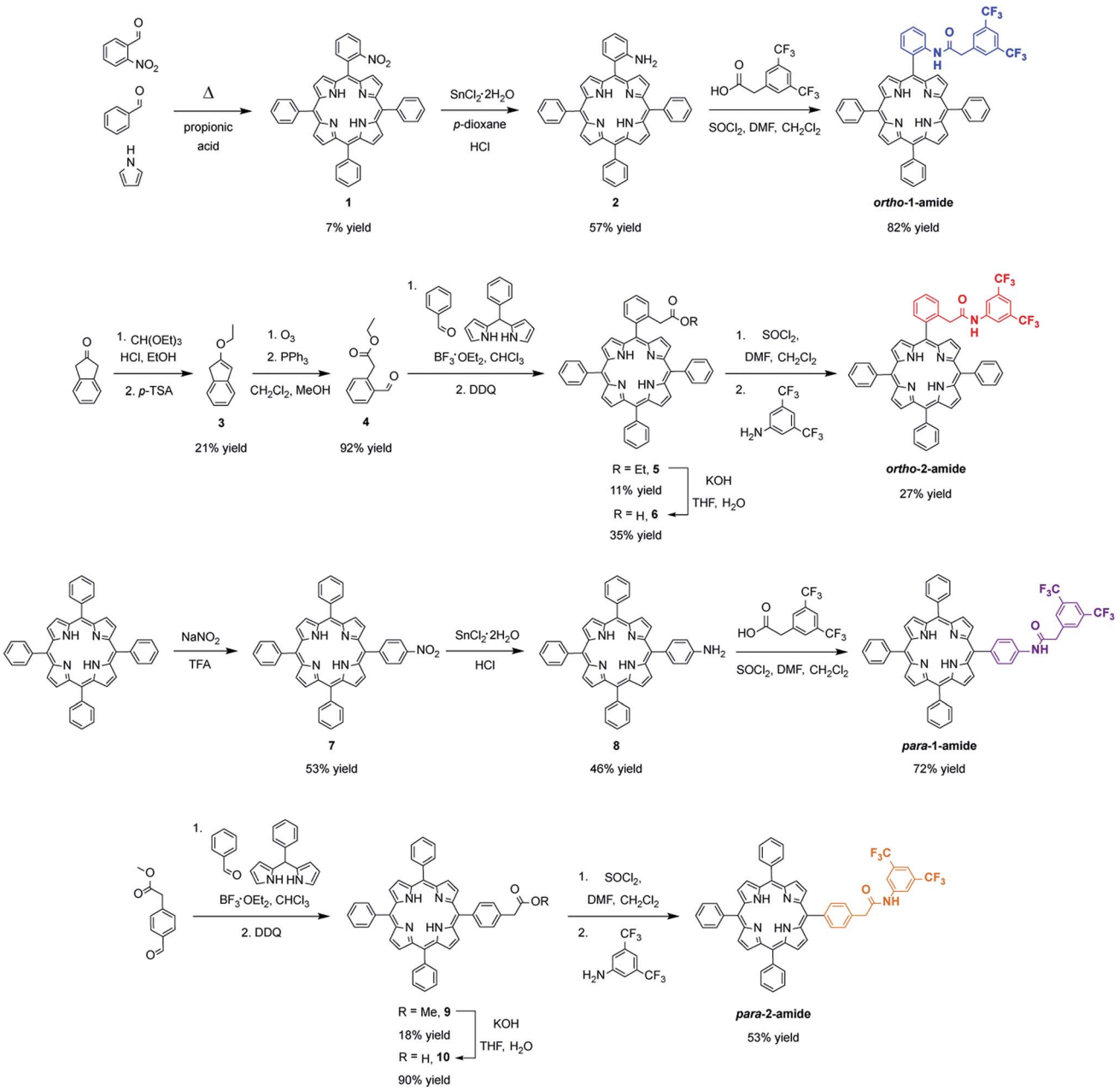

Scheme 2 Synthesis of *ortho*- and *para*-functionalized tetraphenylporphyrin ligands ***ortho*-1-amide**, ***ortho*-2-amide**, ***para*-1-amide**, and ***para*-2-amide**.

 This journal is © The Royal Society of Chemistry 2018

Open Access Article. Published on 21 2018. Downloaded on 16.10.2025 18:37:00.
This article is licensed under a Creative Commons Attribution-NonCommercial 3.0 Unported Licence.

mono-(2-aminophenyl)porphyrin synthon **2**. Reaction with 3,5-bis(trifluoromethyl)phenylacyl chloride affords the proximal target ***ortho*-1-amide**. The distal *ortho* congener was prepared by condensation of 2-formylphenylacetic acid ethyl ester **4** (obtained in two steps from 2-indanone) and benzaldehyde with 5-phenyldipyrromethane to afford porphyrin **5**. Subsequent hydrolysis, followed by *in situ* generation of the acyl chloride and reaction with 3,5-bis(trifluoromethyl)aniline affords ***ortho*-2-amide**. Porphyrin ***para*-1-amide** is obtained from mono-(4-aminophenyl)porphyrin **8**, which is in turn prepared by regioselective *para*-nitration of tetraphenylporphyrin and subsequent reduction. A precursor to ***para*-2-amide** was accessed by condensation of commercially available 4-formylphenylacetic acid methyl ester and benzaldehyde with 5-phenyldipyrromethane to afford porphyrin **9**. Hydrolysis, followed by *in situ* generation of the acyl chloride and reaction with 3,5-bis(trifluoromethyl)aniline, gave the desired ligand.

The iron complexes of the aforementioned porphyrin ligands were obtained by metalation with $FeBr_2$ in anhydrous tetrahydrofuran in the presence of 2,6-lutidine as a base. All porphyrin ligands were characterized by ^{1}H-, ^{13}C-, and ^{19}F-NMR spectroscopy, and freebase and metalloporphyrins were additionally characterized by UV-visible spectroscopy and ESI mass spectrometry (see ESI† for details).

Structural characterization of Zn–*ortho*-1-amide

We sought structural characterization of the amide-appended porphyrins to confirm the expected connectivity. Owing to a lack of success in obtaining suitable quality single crystals for structural characterization of the iron complexes, the corresponding zinc complexes were targeted. Porphyrin **Zn–*ortho*-1-amide** was prepared by metalation of the ligand with $Zn(OAc)_2$. Crystals suitable for X-ray diffraction were grown by vapor diffusion of water into a concentrated DMF solution. The solid-state structure is shown in Fig. 2, where a DMF molecule occupies the fifth axial coordination site. As is typical for pentacoordinate Zn porphyrins, the Zn atom is displaced from the porphyrin plane. As desired, the amide is oriented such that it may engage CO_2 directly or act as a proton relay or hydrogen bond donor with CO_2-bound intermediates during catalysis. We have been unable to obtain X-ray quality crystals of **Zn–*ortho*-2-amide**, perhaps due to enhanced flexibility of the amide group caused by the presence of the methylene spacer.

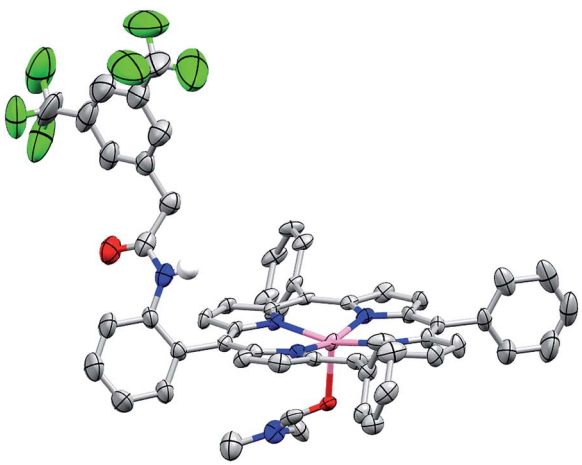

Fig. 2 Solid-state structure of Zn–*ortho*-1-amide. Non-coordinated solvent molecules and non-amide hydrogen atoms have been omitted for clarity. Thermal ellipsoids are shown at the 50% level.

Cyclic voltammetry studies in dimethylformamide

With these positional isomers in hand (Scheme 3), we next evaluated their electrochemical characteristics under an inert atmosphere and under CO_2. Cyclic voltammograms (CVs) of the functionalized iron porphyrins and parent **Fe-TPP** measured in DMF under argon atmosphere (0.1 M $TBAPF_6$, 1 mM catalyst) show three distinct redox events corresponding to formal $Fe^{III/II}$, $Fe^{II/I}$, and $Fe^{I/0}$ couples (Fig. S3†). Reversible $Fe^{I/0}$ couples are observed at a scan rate of 100 mV s^{-1} under these conditions. Scan rate-dependence studies show a linear correlation between peak current and $(\text{scan rate})^{1/2}$, indicating that all the complexes are freely diffusing under non-catalytic conditions (Fig. S4†). The $Fe^{I/0}$ standard potentials, E^0_{cat}, are given in Table 1 for each porphyrin complex. The E^0_{cat} potentials trend with the electron-withdrawing nature of the substituent, with *ortho* substituents exerting a larger electronic effect than *para* substituents: the proximal *ortho* amide is inductively electron-withdrawing, followed by the proximal *para* amide and unsubstituted TPP. The distal amides are rendered electron-donating by the methylene substituent, with the *ortho* positional isomer being more electron-rich than the *para*-substituted analogue.

Under 1 atmosphere of CO_2 and in the presence of phenol as an acid source, catalytic responses indicative of CO_2 reduction are observed by cyclic voltammetry for all catalysts examined. In the presence of 100 mM phenol, **Fe–*ortho*-1-amide** exhibits a slightly more positive catalytic onset than **Fe–*ortho*-2-amide**,

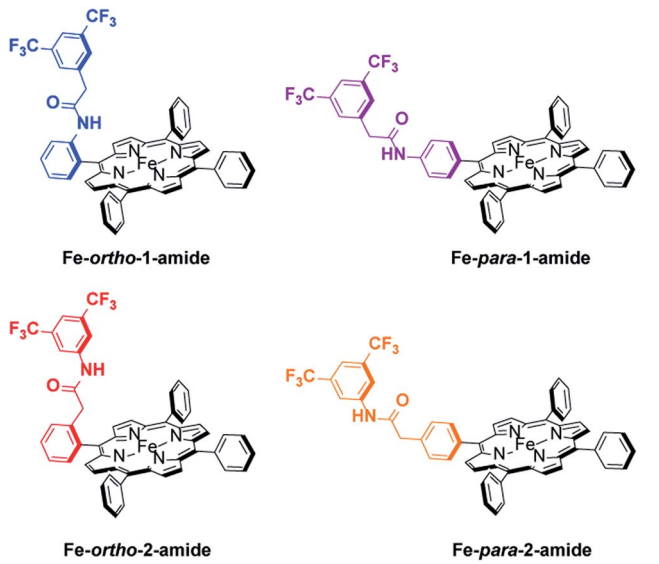

Scheme 3 Positional isomers of amide-functionalized iron tetraphenylporphyrins examined in this work.

Open Access Article. Published on 21 2018. Downloaded on 16.10.2025 18:37:00.
This article is licensed under a Creative Commons Attribution-NonCommercial 3.0 Unported Licence.

Table 1 Summary of electrochemical properties of iron porphyrin catalysts

Catalyst	E^0_{cat} [a] (V *vs.* Fc/Fc$^+$)	TOF_{max} [b] (s^{-1})	log(TOF_{max})	k_{cat} [c] (M^{-2} s^{-1})	FE_{CO} [d] (%)
Fe–*ortho*-1-amide	−2.12	2.24×10^4	4.35	1.01×10^6	83 ± 3
Fe–*ortho*-2-amide	−2.18	5.50×10^6	6.74	3.33×10^8	92 ± 2
Fe–*para*-1-amide	−2.15	1.70×10^2	2.23	1.03×10^4	74 ± 8
Fe–*para*-2-amide	−2.16	6.76×10^3	3.84	4.20×10^5	79 ± 8
Fe-TPP	−2.15	6.76×10^2	2.83	2.13×10^5	90 ± 6
Fe-TPP + 50 mM amide	−2.15	4.04×10^3	3.61	3.18×10^5	—

[a] The standard reduction potential for the formal $Fe^{I/0}$ couple, E^0_{cat}, is reported as an average over three independent experiments. [b] TOF_{max} values are reported in presence of 100 mM PhOH and 0.23 M CO_2 except for the last entry, which is in presence of 50 mM amide additive and 0.23 M CO_2. [c] k_{cat} values are reported as an average over three sets of experimental conditions (different [PhOH], 0.23 M CO_2, in the regime where rate is linearly dependent on [PhOH]). [d] FE for CO is reported as an average over three CPE experiments, see ESI for details.

but both show significantly higher catalytic responses than the corresponding *para*-functionalized positional congeners or unfunctionalized **Fe-TPP** (Fig. 3). In the presence of low phenol concentrations (5 mM), **Fe–*ortho*-2-amide** shows a significantly larger peak current compared to all other catalysts and a comparable onset potential to that of **Fe–*ortho*-1-amide** (Fig. S5†). In contrast, at higher phenol concentrations of 250 mM, **Fe–*ortho*-1-amide** displays a larger peak current and a more anodic onset potential than **Fe–*ortho*-2-amide** (Fig. S5†). These findings suggest that the role of phenol may differ among the positional isomers, or that altered mechanisms of catalyst inactivation are at play.

To gain further insight into CO_2 reduction catalyzed by this series of amide-functionalized porphyrins, the observed rate constants (k_{obs} = TOF_{max}, s^{-1}) determined by FOWA were examined as a function of phenol and CO_2 concentration. Under pseudo-first order conditions, all four functionalized catalysts display first-order dependence on phenol concentration (Fig. 4, S6–13†). **Fe–*ortho*-2-amide** achieves the largest observed rate constants (k_{obs}) of all catalysts tested, but exhibits non-linearity at higher phenol concentrations, possibly as a result of catalyst inhibition or local depletion of CO_2. **Fe–*ortho*-1-amide** exhibits the next highest set of k_{obs} values, followed by **Fe–*para*-2-amide** and finally **Fe–*para*-1-amide**. Maximum turnover frequencies (TOF_{max}) in the presence of 100 mM phenol are summarized in Table 1. Likewise, all four catalysts show first-order dependence on CO_2 concentration in the presence of excess (500 mM) phenol (Fig. S20†), as well as on catalyst concentration (Fig. S21†). Taken together, in the linear regimes of [PhOH] and [CO_2] where secondary phenomena are minimal, all four catalysts follow the rate law

$$\frac{-\mathrm{d}[CO_2]}{\mathrm{d}t} = k_{obs}[cat] = k_{cat}[PhOH][CO_2][cat]$$

where k_{cat} (M^{-2} s^{-1}) is the intrinsic third-order rate constant. Average values for k_{cat}, determined at several phenol concentrations in the linear regime, are reported in Table 1. TOF_{max} and k_{cat} values for unfunctionalized **Fe-TPP** in the presence of 50 mM amide additive are also shown for comparison, demonstrating that *ortho* pendant amide groups are necessary to observe large enhancements in activity.

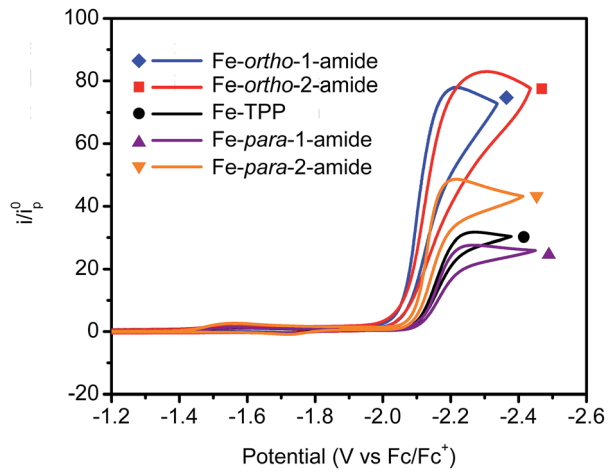

Fig. 3 Cyclic voltammograms of amide-functionalized porphyrins and unfunctionalized **Fe-TPP** under CO_2 atmosphere. Conditions: 1 mM catalyst, 100 mM phenol, 0.1 M $TBAPF_6$ in DMF, saturated with CO_2 (0.23 M); scan rate 100 mV s^{-1}. *i* represents current under catalytic conditions; i^0_p represents the cathodic peak height of the formal $Fe^{II/I}$ couple under inert atmosphere.

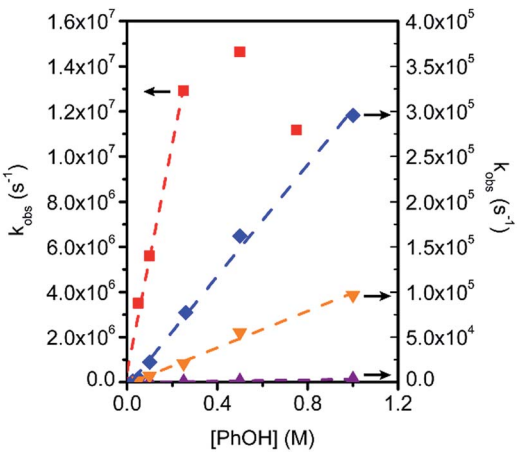

Fig. 4 Observed rate constants (s^{-1}) for catalytic CO_2 reduction as a function of PhOH concentration for **Fe–*ortho*-1-amide** (blue diamonds), **Fe–*ortho*-2-amide** (red squares), **Fe–*para*-1-amide** (purple upward triangles), and **Fe–*para*-2-amide** (orange downward triangles). Conditions: 1 mM catalyst, 0.1 M $TBAPF_6$ in DMF; 0.23 M CO_2; scan rate is 100 mV s^{-1}. k_{obs} values were determined by FOWA.

This journal is © The Royal Society of Chemistry 2018

Open Access Article. Published on 21 2018. Downloaded on 16.10.2025 18:37:00.
This article is licensed under a Creative Commons Attribution-NonCommercial 3.0 Unported Licence.

For the purposes of catalyst benchmarking, it is illustrative to examine the log(TOF) *vs.* overpotential (η) relationships as indicated by a catalytic Tafel plot.[61] More effective catalysts operate with higher TOFs at lower overpotentials and are displayed in the upper left portion of such plots. As shown in Fig. 5, **Fe–*ortho*-2-amide** exhibits higher TOFs over all overpotential values compared to **Fe–*ortho*-1-amide**, which in turn exhibits higher TOFs compared to **Fe-TPP** and both *para*-substituted porphyrins. The values at the plateau of such curves represent $\log(TOF_{max})$, the maximum turnover frequency achievable at large overpotential (when the catalyst is fully present in its reduced state).

The selectivity and stability of the aforementioned catalysts were examined by controlled potential electrolysis (CPE). A solution of catalyst in CO_2-saturated DMF electrolyte (0.1 M $TBAPF_6$, 0.5 mM catalyst, 0.5 M phenol as acid source) was electrolyzed at potentials between −2.1 and −2.2 V *vs.* Fc/Fc^+ in a homemade gas-tight electrolysis cell (see ESI† for details). Gas chromatographic measurements of the headspace reveal that all four amide-functionalized catalysts have high selectivity for CO, with faradaic efficiencies (FE) between 74% and 92% (Tables 1, S2†). No hydrogen was observed for any catalyst under these conditions. Representative CPE traces are provided in Fig. S25.†

Though the previous metrics indicate that **Fe–*ortho*-2-amide** is a superior catalyst compared to **Fe–*ortho*-1-amide**, it is important to stress that the difference in E^0_{cat} values between catalysts must be considered when attempting to resolve questions of optimal second-sphere pendant placement. As illustrated previously,[62,63] electron withdrawing- or donating substituents on the porphyrin aryl rings modulate E^0_{cat} and consequently alter the driving force for electrochemical CO_2 reduction. In such cases, a linear scaling relationship between $\log(TOF_{max})$ and E^0_{cat} is observed, where catalysts having more negative E^0_{cat} values exhibit larger TOFs. Deviation from this relationship occurs when second-sphere interactions either promote or inhibit catalysis, as has been previously documented for electrostatic effects.[64]

In order to benchmark the electronic scaling relationship, **Fe-TPP** and two additional iron porphyrins with no second-sphere influences were investigated: **Fe–*para*-$(CF_3)_4$**, the iron complex of *meso*-tetra(4-trifluoromethylphenyl)porphyrin, and **Fe–*para*-$(OMe)_4$**, the iron complex of *meso*-tetra(4-methoxyphenyl)porphyrin. The synthesis and characterization of these two additional complexes are provided in the ESI.† Cyclic voltammograms of **Fe–*para*-$(CF_3)_4$** and **Fe–*para*-$(OMe)_4$** in the presence of phenol and CO_2 show characteristic responses indicative of CO_2 reduction (Fig. S14, S18†). FOWA was applied to determine TOF_{max} values under conditions identical to those given above for the amide-functionalized porphyrins (Fig. S15, S19†). Controlled potential electrolysis experiments (Fig. S26†) show that CO is also a major product for these two catalysts, with FE_{CO} of 70–74% (Table S2†). The similar product selectivity permits meaningful comparisons with the amide-functionalized complexes. The electrochemical parameters for **Fe–*para*-$(CF_3)_4$** and **Fe–*para*-$(OMe)_4$** are summarized in Table S1.† Together with **Fe-TPP**, these two catalysts exhibit the expected linear relationship between $\log(TOF_{max})$ and E^0_{cat} (circles, Fig. 6).

To examine the contribution of through-space interactions on catalysis by the *ortho*- and *para*-amide-substituted porphyrins, each complex was added to the plot of $\log(TOF_{max})$ *vs.* E^0_{cat} shown in Fig. 6. Both **Fe–*ortho*-1-amide** and **Fe–*ortho*-2-amide** lie significantly above the line corresponding to electronic-only effects, confirming that second-sphere interactions enhance the rate of CO_2 reduction for both complexes. **Fe–*ortho*-2-amide** shows a much larger departure from the electronic correlation line compared to **Fe–*ortho*-1-amide**,

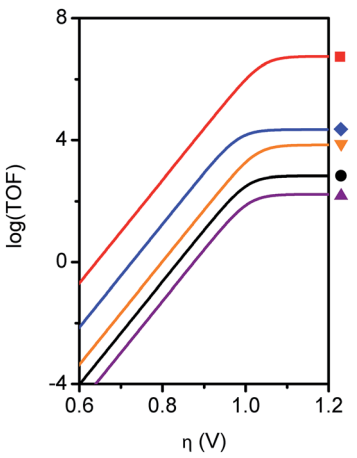

Fig. 5 Catalytic Tafel plots for **Fe–*ortho*-1-amide** (blue diamond), **Fe–*ortho*-2-amide** (red square), **Fe–*para*-1-amide** (purple upward triangle), **Fe–*para*-2-amide** (orange downward triangle), and **Fe-TPP** (black circle). Conditions: 0.1 M $TBAPF_6$ in DMF; 0.23 M CO_2; 100 mM PhOH; scan rate is 100 mV s^{-1}. TOF = k_{obs} and was determined by FOWA.

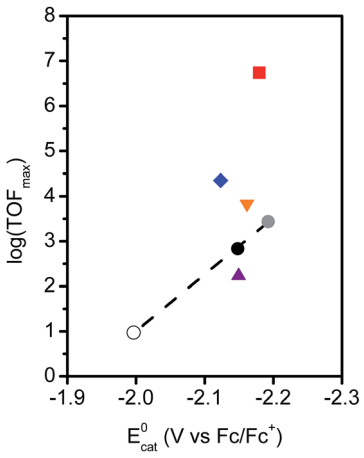

Fig. 6 Correlation between $\log(TOF_{max})$ and E^0_{cat} illustrating the through-space interactions that promote catalysis in the case of **Fe–*ortho*-1-amide** (blue diamond) and **Fe–*ortho*-2-amide** (red square). Porphyrin catalysts with no through-space interactions are shown in black: **Fe–*para*-$(CF_3)_4$** (white circle), **Fe-TPP** (black circle), and **Fe–*para*-$(OMe)_4$** (gray circle). **Fe–*para*-2-amide** (orange downward triangle) and **Fe–*para*-1-amide** (purple upward triangle) show minimal through-space effects. TOF_{max} determined by FOWA in the presence of 100 mM phenol and 0.23 M CO_2.

Open Access Article. Published on 21 2018. Downloaded on 16.10.2025 18:37:00.
This article is licensed under a Creative Commons Attribution-NonCommercial 3.0 Unported Licence.

suggesting that the extent of through-space stabilization of the iron-bound CO_2 adduct is larger for the distal *ortho* isomer than for the proximal congener. In contrast, the $\log(TOF_{max})$ for **Fe–*para*-2-amide** is very slightly higher, and that for **Fe–*para*-1-amide** is very slightly lower, than that predicted by the electronic scaling relationship, suggesting that the *para*-substituted positional isomers do not exhibit notable through-space effects.

In order to gain further insight into the role of the *ortho* amide pendants in promoting catalysis, we determined the equilibrium constants for CO_2 binding, K_{CO_2}, based on the potential shift of the formal $Fe^{I/0}$ couple under Ar and CO_2. These experiments were performed at fast scan rates (2–10 V s^{-1}) in the absence of an added proton source to prevent subsequent catalytic turnover (Fig. S35†). As shown in Table 2, **Fe-TPP** and **Fe–*para*-2-amide**, which lack the ability to engage in productive through-space interactions, exhibit low K_{CO_2} values (2–4 M^{-1}). In contrast, **Fe–*ortho*-1-amide** and **Fe–*ortho*-2-amide** exhibit significantly larger K_{CO_2} values (14–17 M^{-1}), indicating that properly positioned amide pendants act to increase the affinity for CO_2 *via* hydrogen bonding interactions. Quantum chemical calculations on the Fe–CO_2 adducts of both *ortho*-functionalized complexes reveal differences in the length of the amide-CO_2 hydrogen bond (see ESI† for details), with an H–O distance of 1.61 Å for **Fe–*ortho*-1-amide** and 1.45 Å for **Fe–*ortho*-2-amide** (Fig. S39, S40†). The shorter H-bond distance for the latter complex is in agreement with the larger through-space interaction seen electrochemically (Fig. 6).

The role of proton transfer during catalysis was examined by measuring the pK_a values of all four amide pendants, as well as the H/D kinetic isotope effects. The pK_a values of all four amide pendants were determined spectrophotometrically (Fig. S36–38†) in DMSO, as shown in Table 2. Importantly, the amide of **Fe–*ortho*-2-amide** is less acidic (pK_a = 19.3 ± 0.1) than that of **Fe–*ortho*-1-amide** (pK_a = 18.7 ± 0.2). Thus, the higher catalytic activity of **Fe–*ortho*-2-amide** cannot be ascribed simply to a more acidic amide pendant. In addition, kinetic isotope effects for all four positional isomers were measured using H_2O or D_2O as the proton source (Fig. S20–S27†). Normal primary H/D kinetic isotope effects were observed for all four amide-functionalized catalysts (k_H/k_D between 1.47 and 1.88, see Table 2), suggesting that proton transfer is involved in the rate-determining step regardless of amide positioning.

Table 2 Summary of equilibrium CO_2 binding constants (K_{CO_2}), amide pK_a values, and kinetic isotope effects (KIE) for the iron porphyrin catalysts

Catalyst	K_{CO_2}[a] (M^{-1})	Amide pK_a	KIE[b]
Fe-TPP	2.3	N/A	1.5–2.5[c]
Fe–*ortho*-1-amide	17.1	18.7 ± 0.2	1.47
Fe–*ortho*-2-amide	14.4	19.3 ± 0.1	1.77
Fe–*para*-1-amide	—	18.8 ± 0.1	1.88
Fe–*para*-2-amide	3.6	18.7 ± 0.5	1.84

[a] The binding constant for **Fe–*para*-1-amide** could not be measured but is expected to be between 2–4 M^{-1}. [b] KIE values represent the ratio of k_H/k_D measured using water as the proton source (see ESI for details). [c] Values reported for various proton sources, see ref. 65.

These results confirm, unsurprisingly, that second-sphere donors must be located at the *ortho*-positions of the porphyrin scaffold to exhibit productive interactions with catalytically-relevant intermediates. More interestingly, we show that a distally-located second-sphere amide group is more effective at breaking the electronic scaling relationship for CO_2 reduction than the proximal positional isomer due to enhanced hydrogen bond stabilization of the Fe–CO_2 intermediate. Differences in pK_a of the four amide pendants are minimal, indicating that their position with respect to the iron-bound CO_2 is more likely what governs differences in catalytic activity. The primary kinetic isotope effects observed for all four amide-functionalized catalysts are in agreement with those measured with other proton sources[65] or for other CO_2 reduction catalysts,[22] and indicate that proton transfer is involved in the rate-determining step. Given the pK_a of the amide pendants, they are expected to act as proton relays in addition to hydrogen bond donors. We therefore conclude that distal *ortho* positioning allows the pendant to adopt a configuration that is more ideally suited to both hydrogen bond stabilization and proton transfer.

Conclusions

In summary, we investigate the positional dependence of secondary coordination sphere groups on the reactivity of a conserved primary iron porphyrin core for electrochemical CO_2 reduction. To this end, four positional isomers were synthesized, varying the location of the second-sphere amide group *ortho*- and *para*-, as well as proximal and distal, to the porphyrin plane. Cyclic voltammetry and controlled potential electrolysis were used to fully characterize the electrochemical behaviour of this family of functionalized porphyrins, including kinetic parameters, catalytic Tafel plots, and faradaic efficiencies for the product CO. Studying the correlation between $\log(TOF_{max})$ and the $Fe^{I/0}$ standard potential, E^0_{cat}, reveals that through-space interactions enhance the rate of catalysis in both *ortho*-functionalized positional isomers, with the distally-located amide exhibiting a more significant enhancement. In contrast, the *para*-functionalized congeners display no significant through-space effects. These results demonstrate that fine-tuning the location of second-sphere pendants is an effective design strategy for the development of highly-active biomimetic catalysts for CO_2 reduction, and by extension, for a wider range of chemical transformations.

Conflicts of interest

There are no conflicts to declare.

Acknowledgements

We thank DOE/LBNL Grant 101528-002 for funding this research. C. J. C. is an Investigator with the Howard Hughes Medical Institute and a CIFAR Senior Fellow. E. M. N. and P. T. S. acknowledge the NSF for graduate research fellowships. S. K. N. thanks the UC Berkeley College of Chemistry for a summer

 This journal is © The Royal Society of Chemistry 2018

Open Access Article. Published on 21 2018. Downloaded on 16.10.2025 18:37:00.
This article is licensed under a Creative Commons Attribution-NonCommercial 3.0 Unported Licence.

undergraduate research award. We acknowledge the National Institutes of Health for funding the UC Berkeley CheXray X-ray crystallographic facility under the Shared Instrumentation Grant S10-RR027172. We also thank Micah S. Ziegler for helpful discussions.

Notes and references

1 A. M. Appel, J. E. Bercaw, A. B. Bocarsly, H. Dobbek, D. L. DuBois, M. Dupuis, J. G. Ferry, E. Fujita, R. Hille, P. J. A. Kenis, C. A. Kerfeld, R. H. Morris, C. H. F. Peden, A. R. Portis, S. W. Ragsdale, T. B. Rauchfuss, J. N. H. Reek, L. C. Seefeldt, R. K. Thauer and G. L. Waldrop, *Chem. Rev.*, 2013, **113**, 6621–6658.

2 E. E. Benson, C. P. Kubiak, A. J. Sathrum and J. M. Smieja, *Chem. Soc. Rev.*, 2009, **38**, 89–99.

3 A. J. Morris, G. J. Meyer and E. Fujita, *Acc. Chem. Res.*, 2009, **42**, 1983–1994.

4 K. H. Takahashi, K. Hiratsuka, H. Sasaki and S. Toshima, *Chem. Lett.*, 1979, **8**, 305–308.

5 M. Hammouche, D. Lexa, J. M. Savéant and M. Momenteau, *J. Electroanal. Chem. Interfacial Electrochem.*, 1988, **249**, 347–351.

6 M. Hammouche, D. Lexa, M. Momenteau and J. M. Saveant, *J. Am. Chem. Soc.*, 1991, **113**, 8455–8466.

7 I. Bhugun, D. Lexa and J.-M. Savéant, *J. Am. Chem. Soc.*, 1996, **118**, 1769–1776.

8 D. D. Behar, T. Dhanasekaran, P. Neta, C. M. Hosten, D. Ejeh, P. Hambright and E. Fujita, *J. Phys. Chem. A*, 1998, **102**, 2870–2877.

9 B. J. Fisher and R. Eisenberg, *J. Am. Chem. Soc.*, 1980, **102**, 7361–7363.

10 A. H. A. Tinnemans, T. P. M. Koster, D. H. M. W. Thewissen and A. Mackor, *Recl. Trav. Chim. Pays-Bas*, 1984, **103**, 288–295.

11 M. Beley, J.-P. Collin, R. Ruppert and J.-P. Sauvage, *J. Chem. Soc., Chem. Commun.*, 1984, 1315–1316.

12 M. Beley, J. P. Collin, R. Ruppert and J. P. Sauvage, *J. Am. Chem. Soc.*, 1986, **108**, 7461–7467.

13 E. C. Fujita, C. Creutz, N. Sutin and D. J. Szalda, *J. Am. Chem. Soc.*, 1991, **113**, 343–353.

14 J. Schneider, H. Jia, K. Kobiro, D. E. Cabelli, J. T. Muckerman and E. Fujita, *Energy Environ. Sci.*, 2012, **5**, 9502–9510.

15 D. C. M. Lacy, C. C. L. McCrory and J. C. Peters, *Inorg. Chem.*, 2014, **53**, 4980–4988.

16 J. Hawecker, J.-M. Lehn and R. Ziessel, *J. Chem. Soc., Chem. Commun.*, 1984, 328–330.

17 J. Hawecker, J.-M. Lehn and R. Ziessel, *Helv. Chim. Acta*, 1986, **69**, 1990–2012.

18 B. P. Sullivan and T. J. Meyer, *J. Chem. Soc., Chem. Commun.*, 1984, 1244–1245.

19 C. M. Bolinger, N. Story, B. P. Sullivan and T. J. Meyer, *Inorg. Chem.*, 1988, **27**, 4582–4587.

20 H. T. Ishida, K. Tanaka and T. Tanaka, *Organometallics*, 1987, **6**, 181–186.

21 M. Bourrez, F. Molton, S. Chardon-Noblat and A. Deronzier, *Angew. Chem., Int. Ed.*, 2011, **50**, 9903–9906.

22 J. M. Smieja, E. E. Benson, B. Kumar, K. A. Grice, C. S. Seu, A. J. M. Miller, J. M. Mayer and C. P. Kubiak, *Proc. Natl. Acad. Sci. U. S. A.*, 2012, **109**, 15646–15650.

23 M. D. N. Sampson, A. D. Nguyen, K. A. Grice, C. E. Moore, A. L. Rheingold and C. P. Kubiak, *J. Am. Chem. Soc.*, 2014, **136**, 5460–5471.

24 S. W. Slater and J. H. Wagenknecht, *J. Am. Chem. Soc.*, 1984, **106**, 5367–5368.

25 D. L. DuBois, A. Miedaner and R. C. Haltiwanger, *J. Am. Chem. Soc.*, 1991, **113**, 8753–8764.

26 P. Kang, T. J. Meyer and M. Brookhart, *Chem. Sci.*, 2013, **4**, 3497–3502.

27 V. S. Thoi and C. J. Chang, *Chem. Commun.*, 2011, **47**, 6578–6580.

28 V. S. K. Thoi, N. Kornienko, C. G. Margarit, P. Yang and C. J. Chang, *J. Am. Chem. Soc.*, 2013, **135**, 14413–14424.

29 J. Agarwal, T. W. Shaw, C. J. Stanton, G. F. Majetich, A. B. Bocarsly and H. F. Schaefer, *Angew. Chem., Int. Ed.*, 2014, **53**, 5152–5155.

30 B. Mondal, J. Song, F. Neese and S. Ye, *Curr. Opin. Chem. Biol.*, 2015, **25**, 103–109.

31 C. L. Drennan, J. Heo, M. D. Sintchak, E. Schreiter and P. W. Ludden, *Proc. Natl. Acad. Sci. U. S. A.*, 2001, **98**, 11973–11978.

32 J.-H. Jeoung and H. Dobbek, *Science*, 2007, **318**, 1461–1464.

33 W. Gong, B. Hao, Z. Wei, D. J. Ferguson, T. Tallant, J. A. Krzycki and M. K. Chan, *Proc. Natl. Acad. Sci. U. S. A.*, 2008, **105**, 9558–9563.

34 J. P. Collman, R. R. Gagne, C. Reed, T. R. Halbert, G. Lang and W. T. Robinson, *J. Am. Chem. Soc.*, 1975, **97**, 1427–1439.

35 J. P. Collman, X. Zhang, K. Wong and J. I. Brauman, *J. Am. Chem. Soc.*, 1994, **116**, 6245–6251.

36 G. E. Wuenschell, C. Tetreau, D. Lavalette and C. A. Reed, *J. Am. Chem. Soc.*, 1992, **114**, 3346–3355.

37 M. Momenteau and C. A. Reed, *Chem. Rev.*, 1994, **94**, 659–698.

38 C. K. Chang, Y. Liang, G. Aviles and S.-M. Peng, *J. Am. Chem. Soc.*, 1995, **117**, 4191–4192.

39 C. J. Chang, L. L. Chng and D. G. Nocera, *J. Am. Chem. Soc.*, 2003, **125**, 1866–1876.

40 A. Wada, M. Harata, K. Hasegawa, K. Jitsukawa, H. Masuda, M. Mukai, T. Kitagawa and H. Einaga, *Angew. Chem., Int. Ed.*, 1998, **37**, 798–799.

41 A. H. Wada, Y. Honda, S. Yamaguchi, S. Nagatomo, T. Kitagawa, K. Jitsukawa and H. Masuda, *Inorg. Chem.*, 2004, **43**, 5725–5735.

42 C. E. MacBeth, A. P. Golombek, V. G. Young, C. Yang, K. Kuczera, M. P. Hendrich and A. S. Borovik, *Science*, 2000, **289**, 938–941.

43 R. L. Z. Lucas, M. K. Zart, J. Mukerjee, T. N. Sorrell, D. R. Powell and A. S. Borovik, *J. Am. Chem. Soc.*, 2006, **128**, 15476–15489.

44 R. L. Shook and A. S. Borovik, *Inorg. Chem.*, 2010, **49**, 3646–3660.

45 S. A. Cook and A. S. Borovik, *Acc. Chem. Res.*, 2015, **48**, 2407–2414.

Open Access Article. Published on 21 2018. Downloaded on 16.10.2025 18:37:00.
This article is licensed under a Creative Commons Attribution-NonCommercial 3.0 Unported Licence.

46 L. M. Berreau, M. M. Makowska-Grzyska and A. M. Arif, *Inorg. Chem.*, 2001, **40**, 2212–2213.
47 M. M. J. Makowska-Grzyska, P. C. Jeppson, R. A. Allred, A. M. Arif and L. M. Berreau, *Inorg. Chem.*, 2002, **41**, 4872–4887.
48 E. M. Matson, Y. J. Park and A. R. Fout, *J. Am. Chem. Soc.*, 2014, **136**, 17398–17401.
49 C. M. Moore and N. K. Szymczak, *Chem. Sci.*, 2015, **6**, 3373–3377.
50 C. L. Ford, Y. J. Park, E. M. Matson, Z. Gordon and A. R. Fout, *Science*, 2016, **354**, 741–743.
51 S. E. Creutz and J. C. Peters, *Chem. Sci.*, 2017, **8**, 2321–2328.
52 M. L. Helm, M. P. Stewart, R. M. Bullock, M. R. DuBois and D. L. DuBois, *Science*, 2011, **333**, 863–866.
53 J. Y. Yang, S. E. Smith, T. Liu, W. G. Dougherty, W. A. Hoffert, W. S. Kassel, M. R. DuBois, D. L. DuBois and R. M. Bullock, *J. Am. Chem. Soc.*, 2013, **135**, 9700–9712.
54 A. Rana, B. Mondal, P. Sen, S. Dey and A. Dey, *Inorg. Chem.*, 2017, **56**, 1783–1793.
55 D. K. Dogutan, R. McGuire and D. G. Nocera, *J. Am. Chem. Soc.*, 2011, **133**, 9178–9180.
56 C. T. M. Carver, B. D. Matson and J. M. Mayer, *J. Am. Chem. Soc.*, 2012, **134**, 5444–5447.
57 C. Costentin, S. Drouet, M. Robert and J.-M. Savéant, *Science*, 2012, **338**, 90–94.
58 A. Chapovetsky, T. H. Do, R. Haiges, M. K. Takase and S. C. Marinescu, *J. Am. Chem. Soc.*, 2016, **138**, 5765–5768.
59 S. Roy, B. Sharma, J. Pécaut, P. Simon, M. Fontecave, P. D. Tran, E. Derat and V. Artero, *J. Am. Chem. Soc.*, 2017, **139**, 3685–3696.
60 C. Costentin, G. Passard, M. Robert and J.-M. Savéant, *Proc. Natl. Acad. Sci. U. S. A.*, 2014, **111**, 14990–14994.
61 C. Costentin, S. Drouet, M. Robert and J.-M. Savéant, *J. Am. Chem. Soc.*, 2012, **134**, 11235–11242.
62 I. Azcarate, C. Costentin, M. Robert and J.-M. Savéant, *J. Phys. Chem. C*, 2016, **120**, 28951–28960.
63 M. L. Pegis, B. A. McKeown, N. Kumar, K. Lang, D. J. Wasylenko, X. P. Zhang, S. Raugei and J. M. Mayer, *ACS Cent. Sci.*, 2016, **2**, 850–856.
64 I. Azcarate, C. Costentin, M. Robert and J.-M. Savéant, *J. Am. Chem. Soc.*, 2016, **138**, 16639–16644.
65 C. Costentin, S. Drouet, G. Passard, M. Robert and J.-M. Savéant, *J. Am. Chem. Soc.*, 2013, **135**, 9023–9031.

This journal is © The Royal Society of Chemistry 2018